Measurements of photon interference X-ray absorption fine structure (πXAFS)

Larc Tröger,* Peter Kappen, Yoshinori Nishino,† Nils Haack and Gerhard Materlik

Hamburger Synchrotronstrahlungslabor HASYLAB at Deutsches Elektronen-Synchrotron DESY, Notkestrasse 85, D-22607 Hamburg, Germany. E-mail: larc.troeger@desy.de

Experimental data are presented which demonstrate the existence of a fine structure in extended X-ray absorption spectra due to interference effects in the initial photon state (πXAFS). Interference occurs between the incident electromagnetic wave and its coherently scattered waves from neighboring atoms. Using fine platinum and tungsten powders as well as polycrystalline platinum foil, πXAFS was measured in high-precision absorption experiments at beamline X1 at HASYLAB/DESY over a wide energy range. πXAFS is observed below and above absorption-edge positions in both transmission and total-electron-yield detection. Based on experimental data it is shown that πXAFS is sensitive to geometric atomic structure. Fourier-transformed πXAFS data carry information, comparable with that of EXAFS, about the short-range-order structure of the sample. Sharp structures occur in πXAFS when a Bragg backscattering condition of the incident X-rays is fulfilled. They allow precise measurement of long-range-order structural information. Measured data are compared with simulations based on πXAFS theory. Although πXAFS structures are similarly observed in two detection techniques, the importance of scattering off the sample for the measurements needs to be investigated further. Disentangling πXAFS, multi-electron photoexcitations and atomic XAFS in high-precision measurements close to absorption edges poses a challenge for future studies.

Keywords: photon interference; initial photon state; XAFS; πXAFS; platinum; tungsten.

1. Introduction

Near and above absorption edges, the absorption coefficient exhibits a fine structure (XAFS) induced by the electronic and geometrical environment of the absorbing atom. It results from the interference of the excited outgoing photoelectron wave with its backscattered waves from neighboring atoms. In conventional formalism, the initial-state photon is assumed to be a plane wave. Extended XAFS (EXAFS) measures in terms of structural information the radial distribution of neighboring atoms, coordination numbers and averaged phonon properties on a short-range-order scale. In this paper we discuss measurements of a new fine structure in the X-ray absorption coefficient which we call photon interference X-ray absorption fine structure (πXAFS). In πXAFS, the initial-state photon is an interference field resulting from the incident electromagnetic wave and its coherently scattered waves from neighboring atoms (see inset of Fig. 2). πXAFS extends over a wide photon energy range since photon interference occurs independently of absorption-edge position. It is shown that πXAFS carries information about the short-range-order structure of the sample, comparable with EXAFS data. Owing to the longer mean free path of a photon compared with the probing photoelectron in EXAFS, πXAFS is also sensitive to longer-range order. Sharp peaks/structures appear at an incident wavelength where Bragg diffraction in the backward direction occurs.

2. Theory

Recently it has been recognized that even far from Bragg diffraction conditions the photon interference effect produces an observable oscillation in the extended absorption spectrum (Nishino & Materlik, 1999, 2000). This photon interference effect is, for example, used in multiple-energy X-ray holography (MEXH) to obtain three-dimensional atomic structure (Gog *et al.*, 1996).

2.1. *Sample with preferred orientation*

In the work of Nishino & Materlik (1999, 2000), the photoionization cross section for a sample with a preferred orientation is calculated in quantum electrodynamics (QED) including the initial-state photon interaction and the final-state photoelectron interaction with neighboring atoms. The photoionization total cross section, explaining MEXH as well as EXAFS, is given by

$$\sigma_{\rm PI}(E_{\rm x}, \hat{\mathbf{k}}_{\rm x}, \varepsilon) = \sigma_0(E_{\rm x})\big[1 + \chi^{\rm x}(E_{\rm x}, \hat{\mathbf{k}}_{\rm x}, \varepsilon) + \chi^{\rm e}(E_{\rm x}, \varepsilon)\big], \qquad (1)$$

where $E_{\rm x}$, $\mathbf{k}_{\rm x} = k_{\rm x}\hat{\mathbf{k}}_{\rm x}$, and ε are incident photon energy, wavevector, and polarization vector, respectively. $\sigma_0(E_{\rm x})$ is the leading order contribution in QED perturbative expansion and represents the absorption of the isolated atom. $\chi^{\rm x}$ and $\chi^{\rm e}$ are oscillating functions in energy due to interference of X-rays and photoelectrons, respectively. The explicit expressions in the single-scattering plane-wave approximation are given by‡

$$\chi^{\rm x}(E_{\rm x}, \hat{\mathbf{k}}_{\rm x}, \varepsilon) = -2r_{\rm e}{\rm Re}\sum_{i\neq 0}\big[1 - (\varepsilon\cdot\hat{\mathbf{r}}_i)^2\big] \times \frac{f_i^{\rm x}(|\mathbf{k}_{\rm x} + k_{\rm x}\mathbf{r}_i|)}{r_i}\exp\big[i\,(k_{\rm x}r_i + \mathbf{k}_{\rm x}\cdot\mathbf{r}_i)\big], \qquad (2)$$

and

$$\chi^{\rm e}(E_{\rm x}, \varepsilon) = -\frac{3}{k_{\rm e}}\sum_{i\neq 0}\frac{(\varepsilon\cdot\hat{\mathbf{r}}_i)^2}{r_i^2}{\rm Im}\big[f_i^{\rm e}(2k_{\rm e})\exp(2ik_{\rm e}r_i)\big], \qquad (3)$$

where $r_{\rm e}$ is the classical electron radius, $\mathbf{k}_{\rm e} = k_{\rm e}\hat{\mathbf{k}}_{\rm e}$ is the photoelectron wavevector, and $\mathbf{r}_i = r_i\hat{\mathbf{r}}$ is a position vector of the ith neighboring atom measured from the absorbing atom. The sums over i run over all atoms in the system except the absorbing atom. $f_i^{\rm x}$ is the atomic form factor of the photon scattering, $f_i^{\rm e}$ the scattering amplitude of the electron scattering from the ith atom. $2k_{\rm e}$ in the argument of the electron–atom scattering amplitude $f_i^{\rm e}$ denotes the backscattering geometry. The photon interference contribution $\chi^{\rm x}$ of (2) is responsible for MEXH (Nishino & Materlik, 1999, 2000; Adams *et al.*, 1998). The photoelectron interference contribution $\chi^{\rm e}$ of (3) is the leading (single-scattering) contribution of EXAFS (Prins & Koningsberger, 1988, and references therein). Although the photon interference effect $\chi^{\rm x}$ has not been considered in present EXAFS theory, it can contribute considerably. For a perfect crystal near a Bragg diffraction condition, the single scattering approximation in (2) is no longer appropriate because of strong multiple scattering. Dynamical theory of X-ray diffraction becomes necessary.

† On leave from Japan Synchrotron Radiation Research Institute (JASRI), 1-1-1 Kouto, Mikazuki-cho, Sayo-gun, Hyogo 679-5198, Japan.

‡ Note that $\bar{\chi}^{\rm x}$ and $\bar{\chi}^{\rm e}$ in the paper by Nishino & Materlik (1999, 2000) are respectively equivalent to $-\chi^{\rm x}$ and $-\chi^{\rm e}$ in this work.

2.2. *Sample with averaged orientation*

If a sample is polycrystalline, amorphous or non-solid, the photoionization total cross section, equation (1), needs to be averaged over the neighbor orientations $\hat{\mathbf{r}}_i$. The neighbor orientation random average $\bar{\chi}^{\rm e}$ of the photoelectron interference contribution $\chi^{\rm e}$ is simply given by (3) by replacing the factor $(\varepsilon \cdot \hat{\mathbf{r}}_i)^2$ by 1/3. By using a similar calculation procedure as for the EXAFS calculations in the work of Lee (1976), one obtains for the random average of the photon interference contribution $\chi^{\rm x}$ the expression (Nishino & Materlik, 2001)

$$\bar{\chi}^{\rm x}(E_{\rm x}) = -\frac{r_{\rm e}}{k_{\rm x}} \sum_{i\neq 0} \frac{1}{r_i^2} \mathrm{Im}\left[f_i^{\rm x}(2k_{\rm x}) \exp(2ik_{\rm x} r_i) \right]. \qquad (4)$$

Therefore, after angular averaging, only backward scattering contributions remain. $\bar{\chi}^{\rm x}$ oscillates with the phase $2k_{\rm x}r_i$. In (4), higher-order terms in $(k_{\rm x}r_i)^{-1}$ were neglected by assuming that the incident X-ray wavelength is smaller than the interatomic distances. The X-ray polarization ε-dependent term in (2) results in higher-order terms in $(k_{\rm x}r_i)^{-1}$ after $\hat{\mathbf{r}}_i$ averaging.

2.3. *Comparison of πXAFS and EXAFS*

πXAFS $\bar{\chi}^{\rm x}$ of (4) and EXAFS $\bar{\chi}^{\rm e}$ are of equivalent form. It is important to note that the πXAFS oscillation $\bar{\chi}^{\rm x}$ is periodic in photon wavenumber $k_{\rm x}$, and therefore is in incident X-ray energy ($E_{\rm x} = \hbar c k_{\rm x}$). The EXAFS oscillation $\bar{\chi}^{\rm e}$ is periodic in photoelectron wavenumber $k_{\rm e}$. Relative amplitudes of both effects measured at identical k values for the same material are $\bar{\chi}^{\rm x}/\bar{\chi}^{\rm e} = r_{\rm e} f^{\rm x}/f^{\rm e}$. For example, for Pt this ratio is around 1×10^{-3} at $k \simeq 12$ Å^{-1}. This implies that in the classical EXAFS range up to a few keV above an absorption edge, EXAFS usually will largely dominate πXAFS structures in samples with averaged orientation. However, the wavenumber of the photoelectron increases rapidly with the incident X-ray energy. Therefore varying scattering amplitude and Debye–Waller factor [not included in (3)] rapidly damp the EXAFS with increasing incident energy. Several keV above an absorption edge, πXAFS effects will dominate EXAFS, because the wavenumber $k_{\rm x}$ of the X-rays increases much slower with incident X-ray energy. Debye–Waller damping and variations of the scattering amplitude of πXAFS are also weaker, implying that πXAFS extends over a wider range of energy than EXAFS does. Furthermore, below K or L_3 absorption edges, EXAFS can be neglected, which allows one to measure 'clean' πXAFS effects.

The frequency of $\bar{\chi}^{\rm x}$ depends on the distance of an atom from the absorbing atom. The slowest oscillation is obtained for the nearest-neighbor distance (*e.g.* periodicity 2.4 keV for a typical bond length of 2.6 Å). Many higher frequencies occur because of the large mean free path of the photon.

Since $\chi^{\rm x}$ is the three-dimensional holographic signal of MEXH, $\bar{\chi}^{\rm x}$ is considered as a one-dimensional (angular-averaged) X-ray hologram. Similarly, EXAFS is regarded as an angular integrated one-dimensional photoelectron hologram.

2.4. *πXAFS simulation*

For a realistic simulation of the angular-averaged πXAFS of (4), a Debye–Waller factor $\exp(-2\sigma^2 k_{\rm x}^2)$ and an attenuation factor $\exp[-2r_i/l_{\rm x}(E_{\rm x})]$ are included. Here, σ^2 is the mean-square relative displacement of atoms, and $l_{\rm x}(E_{\rm x})$ is the photon mean free path. Compared with EXAFS, πXAFS has less contributions from phase shift and multiple scattering, which makes its simulation much simpler. The cluster for the simulation had a radius of 150 Å. For simplicity, correlated atomic motion was neglected, and for the mean-square relative displacements σ^2, twice the value in X-ray diffraction (Macgillavry & Rieck, 1985) was assumed.

3. Experimental

πXAFS signals were measured (Nishino *et al.*, 2000) at the bending-magnet beamline X1 at the Hamburger Synchrotronstrahlungslabor HASYLAB at Deutsches Elektronen-Synchrotron DESY, Germany. This beamline is optimized for high-precision X-ray absorption experiments. The X-rays were monochromated by either a Si(111) or a Si(311) double-crystal monochromator which was detuned to around 50% and stabilized using a remotely controlled digital monochromator stabilization. An optical encoder system precisely measured the monochromator crystal angle with nominal accuracy of around 10^{-5} degrees or 0.035 arcsec. This determines the incident X-ray energy.

High-purity (>99.95%) Pt and W powders of $\leq$1–2 µm particle size (Goodfellow) were attached to adhesive conductive graphite foil of thickness 30 µm. This yields samples with random angular grain/particle orientation. Thickness was varied by stacking up to three of these covered foils. Additionally, high-purity (>99.95%) 12.5 µm and 25 µm-thick Pt foils were measured. The distribution of grain orientations in these polycrystalline foils is not precisely known due to possible texture formation during fabrication. The high purities ensure that signals of the order of 10^{-3} to 10^{-4} are not influenced by impurities.

Measurements were simultaneously performed in transmission and total electron yield (EY) mode at room temperature in the cell shown in Fig. 1. The cell, which is high-vacuum tight, was operated in a dynamical pure-He gas atmosphere (purity 5.0) to achieve a current amplification of the EY signal by means of gas ionization. Both sample and collector current were measured using Keithley amplifiers. The beam passed through a 7 mm diameter hole in the collector ring. The collector was biased to +90 V. The whole setup was attached to two goniometers and placed on an x–y translation stage which

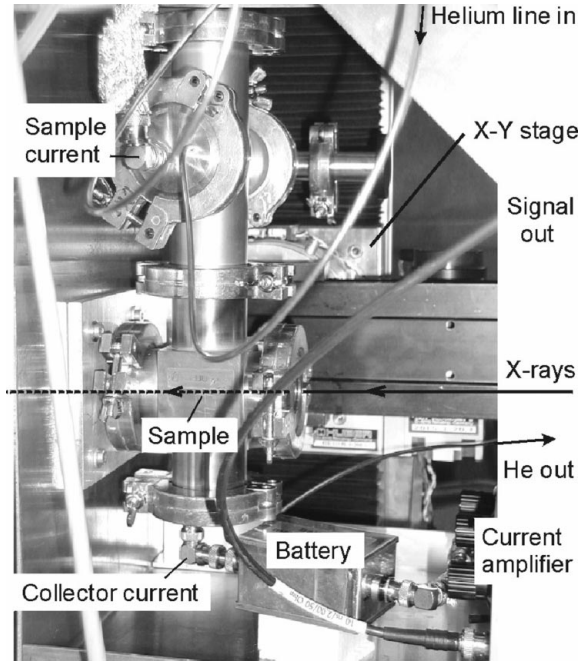

Figure 1
Experimental setup for simultaneous EY and transmission detection.

allows precise adjustment of the cell with respect to the X-ray beam. The intensity of incident and transmitted X-rays was measured by flow ionization chambers using Ar, N_2, Ar/N_2 and Kr gases at atmospheric pressure.

The beam size at the sample position was set to 3.5 mm in the horizontal and 1.0 mm in the vertical direction by means of an exit-slit system in front of the first ionization chamber. Behind this first chamber, an additional stray slit system allows one to adjust its acceptance window for scattered X-rays to a size (typically 6 × 1.5 mm) only slightly larger than the beam. This setup was used for πXAFS measurements below the L_3 absorption edges of Pt and W. Additional transmission πXAFS measurements were performed far above the Pt L_1 edge with larger beam size (10 × 1.5 mm) without the EY cell. The photon flux on the sample in all measurements was around 10^{10} s^{-1} in order to achieve sufficiently good signal-to-noise ratio.

To measure the slow oscillatory contributions of πXAFS, the incident energy was varied over a wide energy range above the Pt L_1 absorption edge, *i.e.* from 14.5 keV to 23.5 keV in 3 eV steps. Specific sharp πXAFS structures below the L_3 absorption edges were scanned with a 0.5–1 eV step width over ranges of 200–2000 eV.

From transmission experiments, the linear absorption coefficient $\mu(E_x)$ was calculated using the relation $\mu d = -\ln[(I_t/I_0)/(I_{t,e}/I_{0,e})]$, where I_0 and I_t are incident and transmitted intensities, respectively, d is the sample thickness, and the subscripts 'e' denote measurements without the Pt sample to subtract all contributions other than that from the sample. The fine structure in the EY data was assumed to be the same as the one in the absorption coefficient. The isolated-atom contribution σ_0 in (1) was modelled by a Victoreen function $c_0 + c_1E_x^{-3} + c_2E_x^{-4}$ (c_0, c_1, c_2: fitting parameters) which was fitted to the data. For the data taken below the L_3 edges, fitting was performed over the full energy range shown in the figures (0.5–1.8 keV). The wide energy range above the L_1 edge was fitted over several regions of 2 keV. It was ensured that the normalized signal $\chi = (\sigma - \sigma_0)/\sigma_0$ connects smoothly between subsequent fitting ranges. Using a test signal, this fitting procedure was shown to be appropriate although the lowest frequency mode of the test signal is partly lost.

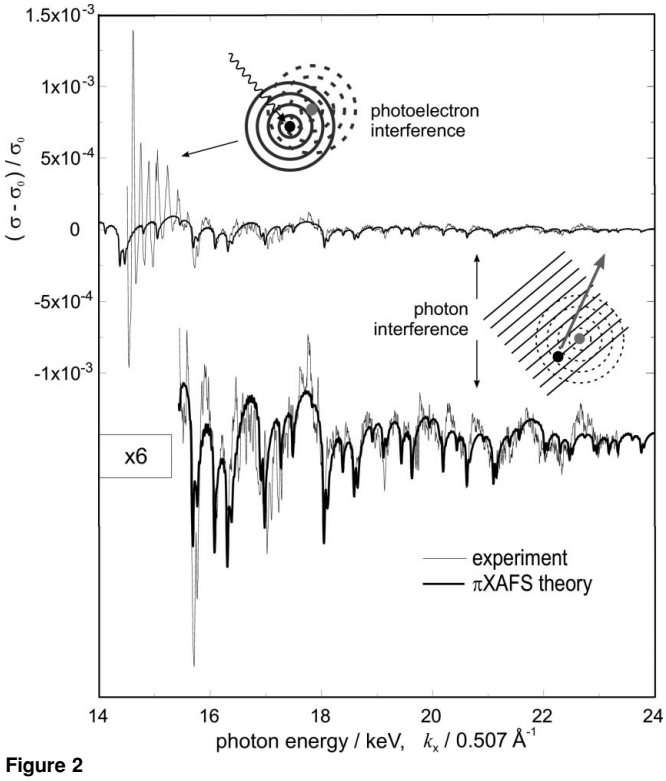

Figure 2
Fine structure of the linear absorption coefficient of a Pt foil. The high-frequency oscillation dominating at energies lower than around 16 keV is the Pt L_1 EXAFS contribution. Above 16 keV, the lower-frequency oscillation and the sharper structures are due to πXAFS (Nishino *et al.*, 2000).

4. Results and discussion

Fig. 2 shows the normalized absorption coefficient $\chi = (\sigma - \sigma_0)/\sigma_0$ of a Pt foil above the L_1 edge measured in transmission. Note the scales of the vertical and horizontal axes. In a plot of the unnormalized data σ (or μd) these small structures are not visible. The high-frequency Pt L_1 EXAFS signal in Fig. 2 fades out as the incident energy increases, and the fine structure of πXAFS becomes dominant in the energy region of around 16 keV and above (Nishino *et al.*, 2000). The lower part of the figure shows the detailed structure of πXAFS in the energy region from 16 keV to 23 keV. The measured signal is in good agreement with the simulation according to (4) including Debye–Waller and attenuation factors. Although the nearest-neighbor contribution to πXAFS is of low frequency, the πXAFS signal in Fig. 2 contains sharp negative peaks because of large contributions from far coordination shells. This will be investigated further in detail below.

Fig. 3 shows the Fourier transform magnitude of $k_x\bar{\chi}^x$ of Fig. 2 with respect to $2k_x$. According to (4), peaks corresponding to radial coordinates of neighbor atoms are expected. This is analogous to the case of EXAFS where a Fourier transform of $\bar{\chi}^e$ (or χ^e) with respect to $2k_e$ shows atomic peaks. The peak positions of the experimental data in Fig. 3 agree well with those from the simulation up to a radial distance of 15 Å. Fig. 3 demonstrates that πXAFS provides direct short-range-order structural information. In this first experiment an accuracy of better than 0.1 Å in determining interatomic distances is achieved. The accuracy of πXAFS with respect to the determination of atomic short-range order is comparable with that of an EXAFS measurement of corresponding k range.

Besides the slow oscillary components of the πXAFS signal leading to the low-r information in the Fourier transform of Fig. 3, the sharp

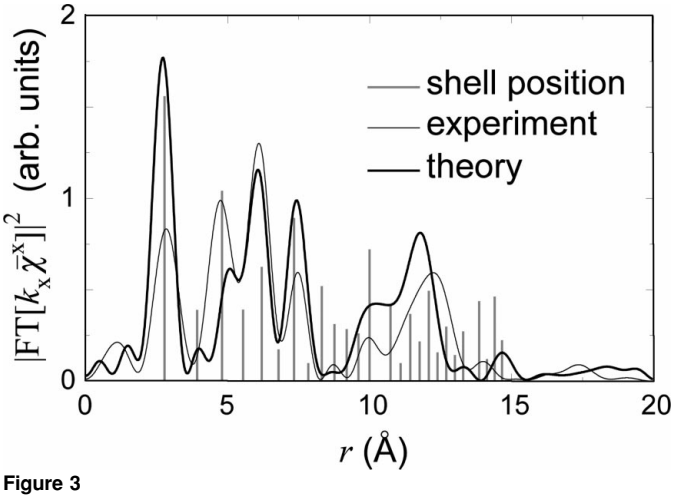

Figure 3
Fourier transform of πXAFS of a Pt foil. The Fourier transformation was performed for the signal $k_x\bar{\chi}^x$ with respect to $2k_x$ in the k_x-range of 8.1 to 11.15 $Å^{-1}$ (energy range 16 to 22 keV). Vertical lines indicate the positions of Pt coordination shells. Their height corresponds to their (weighted) coordination numbers (Nishino *et al.*, 2000).

πXAFS structures are of particular interest. It is noted that the positions of the characteristic sharp structure in πXAFS coincide with the fulfillment of the $\pi/2$ Bragg condition (Nishino & Materlik, 2001). This is more clearly demonstrated in Fig. 4, showing the fine structure of the absorption coefficient of a Pt powder sample measured in transmission more than 1 keV below the L_3 edge. Instead of the smooth atomic behavior, sharp structures occur. They are reproducably observed for different sample preparations, monochromator crystals and detunings.

The energies of these structures do not coincide with any absorption-edge positions. Impurities as their origin therefore can be ruled out. The thin curves in Fig. 4 are πXAFS simulations; vertical lines indicate the energies of Bragg diffraction in backward direction of the incident beam for the lattice planes of given indices. Every set of lattice planes in the f.c.c. crystallites of the Pt powder induces a specific structure in both experiment and theory. Their shape appears to be different in data and simulation. Data show a characteristic, rather step-like, behavior whereas theory yields negative, almost symmetric, peaks. It should be noted that data background subtraction on this level is non-trivial. The least-square fit routine used in the analysis for the determination of the isolated-atom contribution allows larger deviations of the fit at the lower and upper end of the data range. These cutting or edge effects induce the observed larger mismatching with theory at the scan beginning and end.

In a standard transmission experiment, not only true absorption by photoionization is measured, but also scattering off the sample. Since the energy positions of the structures (vertical lines) correspond to the fulfillment of $\pi/2$ backscattering of lattice planes, increasing the incident X-ray energy across these positions in a powder sample always opens up a new Debye–Scherrer cone of scattered X-rays. Even when the scattered X-rays are not entering any detector (*cf.* discussion of Fig. 7*b*), the transmitted intensity is reduced. A step-like increase of the measured linear absorption coefficient is therefore expected at these positions, similar to the experimental observation of Fig. 4.

To investigate the importance of scattering, Fig. 5 compares shape and size of selected πXAFS structures as measured in EY and transmission detection. Also, measurements on a W powder sample with different structure (b.c.c.) are shown. Again, every set of lattice planes induces a specific structure. The absolute units of the vertical scales after normalization allow a quantitative comparison. Both size and shape of the structures are quite similar in all detection modes, and the EY sample and collector current are almost identical. The observed similarity between EY and transmission is noteworthy. Scattered photons are not believed to contribute to the EY signal because no core-hole, photoelectron or secondary electrons are created in the sample. EY is thought to constitute a good measure of the true absorption (photoionization). Close inspection of Fig. 5 may indicate a better agreement of EY data and simulation than of transmission data, but this impression may also be caused by different background shapes. Although the Pt structure at 9350 eV is slightly larger in transmission than in EY (see upper-right of Fig. 5), there is no such general trend (see W data). Positions of minima in theory are shifted to higher energies with respect to experiment. They lie within the step-like increase in the data. A change of lattice constant by 10^{-3} or 0.003 Å would shift the simulation by 10 eV. This implies that πXAFS structures provide accurate long-range-order structural information.

Several other technical checks were performed to ensure that the small structures are not influenced by the particular experimental setup. Firstly, Fig. 6 demonstrates that the πXAFS amplitude measured in transmission is independent of sample thickness. The same is expected and observed for EY. Secondly, Fig. 7 shows measurements of the structures with different monochromator resolution and stray slit size (upper and middle part). As discussed above, a new scattering contribution of X-rays will always induce a positive step in transmission data. However, when a new Debye–Scherrer cone opens up around the backscattering direction, backscattered X-rays might additionally re-enter the first ionization chamber. This would increase its signal, thereby inducing a further positive step in the transmission data. EY would show a negative

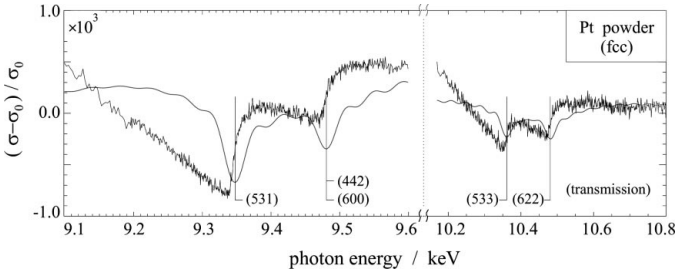

Figure 4
Fine structure of the linear absorption coefficient (πXAFS) of a Pt metal powder sample below the L_3 edge.

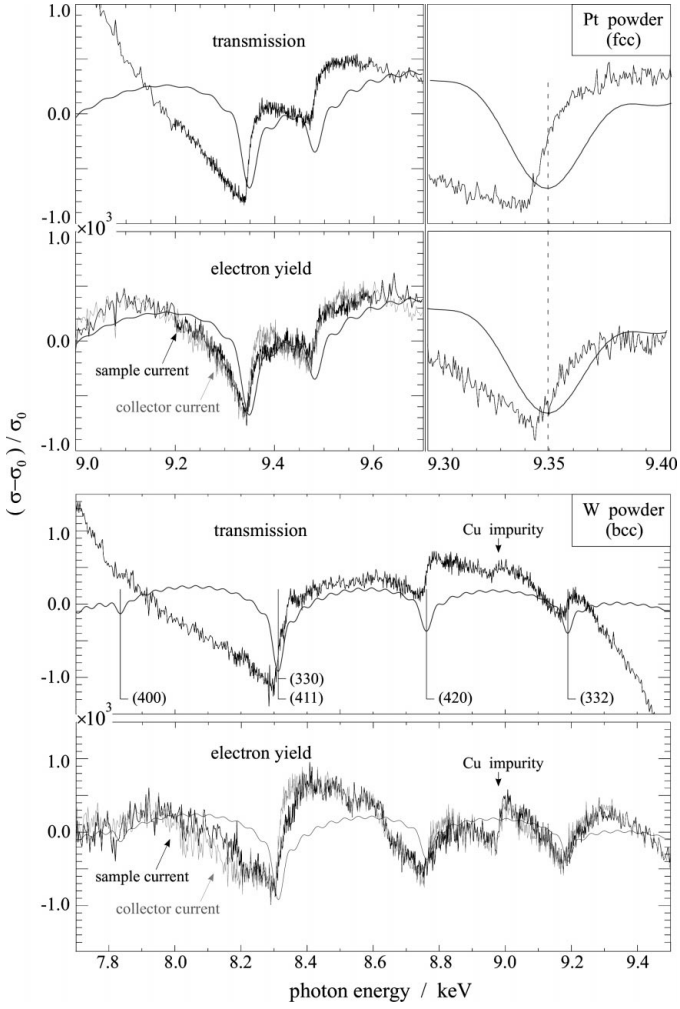

Figure 5
Comparison of simultaneous transmission and EY πXAFS measurements on Pt and W powder samples.

jump instead. In Fig. 7(*b*), the stray slit size determining the acceptance window of the first ionization chamber in backscattering direction to the incident beam was largely varied. No effect on the data is seen.

5. Conclusion and outlook

The results of Figs. 2 and 3 demonstrate that far above an absorption edge, low-frequency oscillations (in comparison with EXAFS frequencies) exist in a standard transmission absorption experiment. They carry direct short-range order information about the atomic structure. Good agreement with a simulation based on πXAFS theory suggests photon interference effects inside the sample as an origin for these oscillations. Because of the much larger mean free path of the X-rays with respect to the probing photoelectron in EXAFS, many higher-frequency components are expected. As the simulation shows, the sharp negative structures visible in Fig. 2 can be explained as a superposition of coherent X-ray scattering contributions from the atomic arrangement inside the Pt f.c.c. crystallites. Although these data are taken far above the L_1 absorption edge where other fine structure like EXAFS is negligible, it is convincing that corresponding specific sharp structures also exist below the lowest L absorption edge (Figs. 4 and 5). Their shape and size are quite similar in different detection techniques, and they carry long-range-order information.

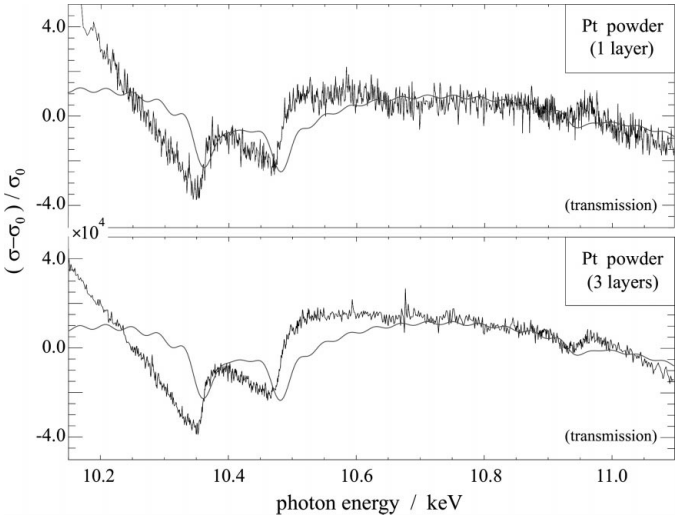

Figure 6
πXAFS transmission data as a function of sample thickness for Pt powder samples.

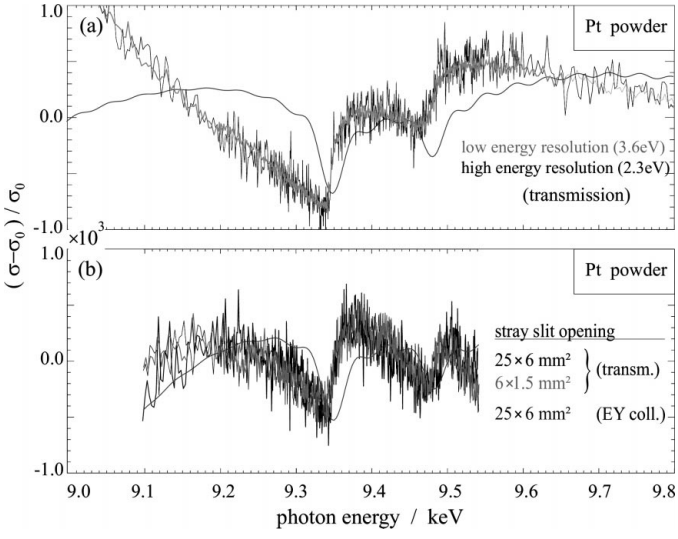

Figure 7
Independence of πXAFS structures on energy resolution and stray slit size for a Pt powder sample.

It is emphasized that, although experimentally observed only recently (Nishino *et al.*, 2000), πXAFS is a general phenomenon providing a new method for determination of atomic structure on short- and longe-range-order scale. Sharp πXAFS structures are anticipated in every crystalline powder sample. From high-accuracy X-ray absorption spectra measured at third-generation synchrotron facilities they may routinely be extracted to yield additional information. However, close to and above absorption edges, πXAFS is a further phenomenon yielding to a fine-structure in the absorption coefficient. Disentangling πXAFS, multielectron photoexcitations and atomic XAFS is a challenge.

The importance of scattering to the observed πXAFS structures is still an open question. The shown πXAFS simulations represent the true absorption because they are based on the calculation of the photoionization cross section. Since true absorption and scattering are intimately linked through Kramers–Kroning transforms, their distinction on the required level here is not easily accessible by experiment. This coupling is in fact used in techniques like X-ray standing wave or diffraction anomalous fine structure measurements. The differences in Figs. 4–7 between experimental data and theory could be explained by scattering contributions off the sample which are not included in the calculation. Step-like scattering contributions are well expected in transmission and would lead to the observed shape in the data. The observed similarity between EY and transmission data, however, then poses the question to which degree EY can be affected by scattering. Possible effects due to extinction should be investigated.

On the other hand, the differences between theory and experiment could be due to imperfections of the theoretical modelling. For example, close to Bragg reflection conditions, where scattering in specific directions is very strong, treatment of multiple-scattering becomes important. In general, theoretical modelling including absorption and scattering processes in view of the specific aspects of each experimental detection technique would be desirable. Further theoretical as well as experimental work is needed to clarify the open questions.

References

Adams, B., Novikov, D. V., Hiort, T., Materlik, G. & Kossel, E. (1998). *Phys. Rev. B*, **57**, 7526–7534.
Gog, T., Len, P. M., Materlik, G., Bahr, D., Fadley, C. S. & Sanchez-Hanke, C. (1996). *Phys. Rev. Lett.* **76**, 3132–3135.
Lee, P. A. (1976). *Phys. Rev. B*, **13**, 5261–5270.
Macgillavry, C. H. & Rieck, G. D. (1985). Editors. *International Tables for X-ray Crystallography*, Vol III. Dordrecht: Kluwer.
Nishino, Y. & Materlik, G. (1999). *Phys. Rev. B*, **60**, 15074–15083
Nishino, Y. & Materlik, G. (2000). *Phys. Rev. B*, **61**, 14845.
Nishino, Y. & Materlik, G. (2001). *J. Synchrotron Rad.* **8**, 203–205.
Nishino, Y., Tröger, L., Korecki, P. & Materlik, G. (2000). Submitted for publication.
Prins, R. & Koningsberger, D. C. (1988). Editors. *X-ray Absorption: Principles, Applications, Techniques of EXAFS, SEXAFS and XANES*. New York: Wiley.

Received 31 July 2000 • Accepted 8 January 2001